

Constraining Hořava-Lifshitz gravity by weak and strong gravitational lensing

Zsolt Horváth,^{*} László Á. Gergely,[†] and Zoltán Keresztes[‡]
*Departments of Theoretical and Experimental Physics,
University of Szeged, Dóm tér 9, Szeged 6720, Hungary*

Tiberiu Harko[§]
*Department of Physics and Center for Theoretical and Computational Physics,
The University of Hong Kong, Pok Fu Lam Road, Hong Kong*

Francisco S. N. Lobo[¶]
*Centro de Astronomia e Astrofísica da Universidade de Lisboa,
Campo Grande, Edifício C8 1749-016 Lisboa, Portugal*

We discuss gravitational lensing in the Kehagias-Sfetsos space-time emerging in the framework of Hořava-Lifshitz gravity. In weak lensing we show that there are three regimes, depending on the value of $\bar{\lambda} = 1/\omega d^2$, where ω is the Hořava-Lifshitz parameter and d characterizes the lensing geometry. When $\bar{\lambda}$ is close to zero, light deflection typically produces two images, as in Schwarzschild lensing. For very large $\bar{\lambda}$ the space-time approaches flatness, therefore there is only one undeflected image. In the intermediate range of $\bar{\lambda}$ only the upper focused image is produced due to the existence of a maximal deflection angle δ_{\max} , a feature inexistent in the Schwarzschild weak lensing. We also discuss the location of Einstein rings, and determine the range of the Hořava-Lifshitz parameter compatible with present day lensing observations. Finally, we analyze in the strong lensing regime the first two relativistic Einstein rings and determine the constraints on the parameter range to be imposed by forthcoming experiments.

PACS numbers: 04.50.Kd, 95.30.Sf, 98.35.Jk, 98.62.Sb

I. INTRODUCTION

Recently, Hořava proposed a renormalizable field theoretical model which can be interpreted as a complete theory of gravity [1, 2]. In the infrared (IR) energy scales, the theory reduces to Einstein gravity with a nonvanishing cosmological constant. However, in the ultraviolet (UV) energy scales, the theory exhibits an anisotropic Lifshitz scaling between time and space given by $x^i \rightarrow lx^i$ and $t \rightarrow l^z t$, where z is the scaling exponent. Due to the latter anisotropic scaling the model is denoted Hořava-Lifshitz gravity in the literature. Taking into account these novel features, Hořava-Lifshitz gravity has received a tremendous amount of attention. As the literature is rather extensive, we refer the reader to [3] for a recent status of the theory. In addition to the formal issues, applications have been extensively explored, ranging from cosmology, dark energy, dark matter to spherically symmetric or rotating solutions.

In fact, several versions of Hořava gravity have been proposed in the literature [3]. The relevant version for cosmology was the introduction of an IR modification term containing an arbitrary cosmological constant, representing the analogs of the standard Schwarzschild-(anti) de Sitter solutions, which were absent in the original Hořava model. In this context, IR-modified Hořava gravity seems to be consistent with the current observational data [4, 5], but in order to test its viability more observational constraints are necessary.

In this work, we discuss the position of images formed in gravitational lensing by the Kehagias-Sfetsos asymptotically flat space-time [6] in the framework of Hořava-Lifshitz gravity. Note that gravitational lensing has become a useful tool in measuring certain properties of gravitational fields and it has now been employed to study the large scale structure of the Universe, to determine behavior of compact stellar objects and to search for dark matter candidates. In what follows we advocate the idea that gravitational lensing might also be used to discriminate which of the various gravitational theories is correct. Indeed, this approach was followed in Ref. [7] in the context of 5-dimensional brane-world theories. In particular, by computing the bending angles and image brightness changes that occur due

^{*}Electronic address: zshorvath@titan.physx.u-szeged.hu

[†]Electronic address: gergely@physx.u-szeged.hu

[‡]Electronic address: zkeresztes@titan.physx.u-szeged.hu

[§]Electronic address: harko@hkucc.hku.hk

[¶]Electronic address: flobo@cii.fc.ul.pt

to the passage of photons past lensing object were determined to distinguish a general relativistic black hole from the black holes predicted by an alternative theory.

We follow the approach proposed in [8], where under some physically realistic assumptions, a simple lens equation was obtained that allows arbitrary small as well as large light deflection angles. This lens equation has been widely used in the literature for studying strong field gravitational lensing. In fact, in the last few years there has been a growing interest in studying weak as well as strong field lensing by a wide plethora of compact objects (we refer the reader to Ref. [9] and references therein and to Refs. [10] for pioneering contributions on strong gravitational lensing).

This paper is organized as follows. In Sec. II, we present the basics of weak lensing in a generic static and spherically symmetric space-time and introduce the relevant notations. In Sec. II C, the image locations in the Kehagias-Sfetsos space-time are analyzed, in particular, the formation of Einstein rings. In Sec. III the weak lensing properties, and in Sec. IV the strong lensing properties of the Kehagias-Sfetsos space-time are analyzed. Finally, in Sec. V we present our conclusions.

II. WEAK LENSING IN KEHAGIAS-SFETSOS GEOMETRY

In this section we summarize the basics of weak lensing in a generic static and spherically symmetric space-time and introduce the relevant notations. The optical axis is defined by the lensing object (L) and the observer (O) (Fig 1). Relative to this axis and seen by O , the source (S) is under angle β , chosen positive by convention (S is always on the upper part of the optical axis). Due to the lensing effect the image of the source (I) appears shifted away. The angle $\theta = \widehat{IOL}$ characterizes the apparent position of the source and it is either positive (for images on the upper side of the optical axis) or negative (for images below the optical axis). Let us denote $s = \text{sgn } \theta$. Finally, the deflection angle $\delta = \widehat{SAI}$ shows the change in the direction of light as compared to an undeflected trajectory. We follow the convention of $\delta > 0$ whenever the light is bent towards the optical axis and $\delta < 0$ otherwise. The projection of both S and I onto the optical axis (N) lies at distance D_{LS} from the lensing object and at D_S from the observer. The observer-lensing object distance therefore is $D_L = D_S - D_{LS}$. We denote $d = D_L D_S / D_{LS}$. The impact parameter is $b = D_L \sin(s\theta)$.

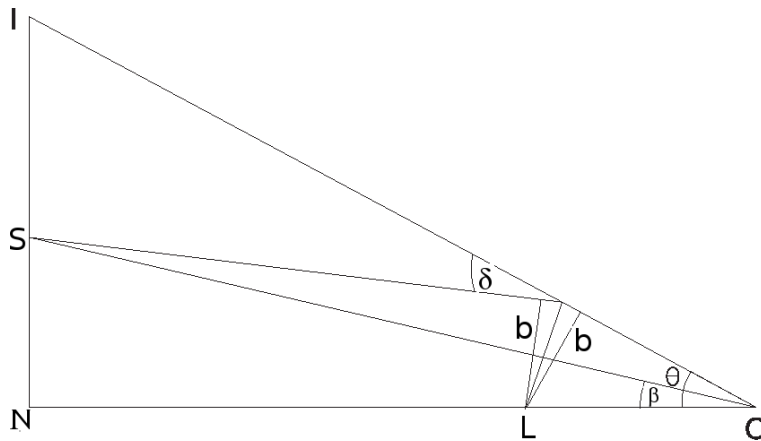


FIG. 1: The lensing geometry for positive apparent angle θ and deflection angle δ .

The deflection angle δ can be calculated by comparing the two asymptotic behaviors of the null geodesics in the $\Theta = \pi/2$ plane, and it is given by the elliptic integral [11]:

$$\delta(r_{\min}) = 2 \int_{r_{\min}}^{\infty} \frac{1}{r} \left[\frac{g_{rr}(r)}{\frac{g_{tt}(r_{\min})}{g_{tt}(r)} \left(\frac{r}{r_{\min}} \right)^2 - 1} \right]^{1/2} dr - \pi, \quad (1)$$

where r_{\min} is the distance of closest approach to the lens:

$$\frac{dr}{d\varphi}(r_{\min}) = 0. \quad (2)$$

A. The Kehagias-Sfetsos geometry

In the framework of Hořava-Lifshitz gravity the geometry of the Kehagias-Sfetsos asymptotically flat space-time [6] is given by the following static and spherically symmetric solution

$$ds^2 = g_{tt}(r) dt^2 + g_{rr}(r) dr^2 + r^2 (d\Theta^2 + \sin^2 \Theta d\varphi^2) , \quad (3)$$

where the metric functions are provided by

$$-g_{tt}(r) = 1/g_{rr}(r) = 1 + \omega r^2 \left[1 - \left(1 + \frac{4GM}{c^2 \omega r^3} \right)^{1/2} \right] , \quad (4)$$

c is the speed of light, G is Newton's constant, M is the total mass of the black hole, and ω is the Hořava-Lifshitz parameter (for details we refer the reader to [6]).

The Kehagias-Sfetsos space-time (4) presents a curvature singularity in the origin. The quantity $\omega_0 = m^2 \omega$ ($m \equiv MG/c^2$) was found useful in [5] for confronting the space-time with Solar System tests. There are two additional coordinate singularities at

$$r_{\pm} = m \left(1 \pm \sqrt{1 - \frac{1}{2\omega_0}} \right) , \quad (5)$$

however they can be transformed away by introducing Eddington-Finkelstein type coordinates (v, r) . The apparent horizon at r_+ , defined by $dr/dv = 0$ (the outer boundary of the trapped region) represents an event horizon, a property which holds in general for stationary space-times. In the limit $\omega_0 \rightarrow \infty$ the outer horizon r_+ approaches the Schwarzschild horizon $2m$ and the inner horizon r_- approaches the central singularity. Unless $\omega_0 \geq \omega_0^{extr} = 1/2$, the solutions r_{\pm} become imaginary, the horizon is absent and the singularity at the origin becomes naked. This does not really represent a restriction on the range of ω_0 , as one can always match the Kehagias-Sfetsos solution with a suitable interior stellar solution at some surface $R_{star} \gg r_+$, similarly as when black hole solutions are employed to describe stellar exteriors.

We note additional difficulties related to the black hole interpretation due to the nonrelativistic dispersion relations, see Ref. [12] with the relevant references and discussion presented there. However, for spherically symmetric solutions of the infrared limit of Hořava-Lifshitz gravity inside the metric horizon there is a universal horizon even in the presence of arbitrarily high propagation speeds [13]. Ref. [14] presents an action principle for Hořava-Lifshitz gravity, based on a Foliation Preserving Diffeomorphisms, according to which massive particles do not follow geodesic paths, however massless particles follow null geodesics. Therefore the expression of the deflection angle (1) can be applied for the light propagating in the Kehagias-Sfetsos space-time (4).

B. Deflection angle and lens equation

By performing a change of variable $\alpha = \arcsin(r_{\min}/r)$, Eq. (1) gives the deflection angle

$$\delta(x_0) = 2 \int_0^{\pi/2} \left[1 + \frac{8(\sin^3 \alpha - 1)(\tan^2 \alpha + 1)\omega_0 x_0}{(16\omega_0^2 x_0^4 + 8\omega_0 x_0 \sin^3 \alpha)^{1/2} + (16\omega_0^2 x_0^4 + 8\omega_0 x_0)^{1/2}} \right]^{-1/2} d\alpha - \pi . \quad (6)$$

When $\omega_0 \rightarrow \infty$ we obtain the Schwarzschild limit of the deflection angle, increasing with $x_0 = r_{\min}/2m$ (the distance of closest approach to the lensing object). By contrast, the limit $\omega_0 \rightarrow 0$ gives a flat space-time and a vanishing deflection angle. With no lens mass there is also no deflection, irrespective of the value of ω , as ω_0 vanishes. The quantities m , x_0 and $\delta(x_0)$ have all the same sign, as in Schwarzschild lensing.

Next we replace the condition (2) with an algebraic equation, following the logic of Ref. [15]. Light-like motions in the equatorial plane of the metric (3) are governed by the Lagrangian

$$2\mathcal{L} = g_{tt}(r) \dot{t}^2 + g_{rr}(r) \dot{r}^2 + r^2 \dot{\varphi}^2 = 0 , \quad (7)$$

the dot representing a derivative with respect to a parameter of the curve. The cyclic coordinates t and φ imply two constants of motion $E = -g_{tt}\dot{t}$ and $L = r^2\dot{\varphi}$. Reinserting these in Eq. (7) we obtain in terms of $u = r^{-1}$ the equation for the trajectory

$$g_{rr}u' = g_{tt}^{-1} \left(\frac{E}{L} \right)^2 - u^2 , \quad (8)$$

where a prime denotes the derivative with respect to φ . The condition (2) gives

$$0 = \left(\frac{L}{E}\right)^2 g_{tt}(r_{\min}) + r_{\min}^2. \quad (9)$$

To zeroth order in the lensing the trajectory would be a straight line with $r_{\min}|_{\text{leading order}} \equiv L/E = b = D_l \sin(s\theta)$. Therefore we could replace the differential condition (2) with the algebraic relation

$$0 = g_{tt}(r_{\min}) D_L^2 \sin^2 \theta + r_{\min}^2. \quad (10)$$

The apparent angle θ , under which an image appears, is found from the Virbhadra-Ellis lens equation [9, 16]:

$$0 = \tan \theta - \tan \beta - \frac{D_{LS}}{D_S} [\tan \theta + \tan(s\delta - \theta)]. \quad (11)$$

The numerical solution of Eqs. (6), (10) and (11), together with the expressions of g_{tt} and g_{rr} gives the loci of the images.

The simplest example for solving the system above is for a Schwarzschild black hole $-g_{tt} = 1 - 2m/r$. After expanding the integrand in Eq. (1), and Eq. (10) in powers of $\bar{\varepsilon}$, to *leading order* we get $\delta = 4m/r_{\min}$ and $\theta = sr_{\min}/D_L$, which together give $\delta = 4m/D_L |\theta|$. The positions of the images are

$$\theta_{1,2} = \frac{\beta}{2} \pm \sqrt{\frac{\beta^2}{4} + 4\bar{\varepsilon}}. \quad (12)$$

In what follows, we will need the position of images for g_{tt} of the Kehagias-Sfetsos space-time.

C. Image locations in the Kehagias-Sfetsos space-time

We first define $\bar{\varepsilon} = m/d$, then by introducing normalized parameters θ/β and $\bar{\varepsilon}/\beta^2$ provided that $\beta \neq 0$, the dependence of the apparent angles from β is eliminated. As for the mass, we also define a useful parameter $\bar{\lambda} = 1/\omega d^2$, encompassing information about the Hořava-Lifshitz parameter ω and the lensing geometry. The parameters $\bar{\varepsilon}$, $\bar{\lambda}$ and ω_0 obey

$$\omega_0 \bar{\lambda} = \bar{\varepsilon}^2. \quad (13)$$

Then this leads to the black hole condition

$$\bar{\varepsilon}^2 \geq \frac{\bar{\lambda}}{2}. \quad (14)$$

The weak gravity sector of the Kehagias-Sfetsos space-time occurs when $-g_{tt} - 1 \ll 1$. This can either occur close to the Schwarzschild limit ($\omega \rightarrow \infty$) or when $\omega \rightarrow 0$ (thus $\bar{\lambda} \rightarrow \infty$). The latter condition renders the geometry outside the black hole parameter region (large $\bar{\lambda}$ and finite m , thus Eq. (14) is not obeyed). In this limit the Kehagias-Sfetsos space-time becomes flat without approximating Schwarzschild, but rather a naked singularity (unless matched with a stellar solution replacing the central region).

Negative mass parameters are allowed only for $1 + 4m/\omega r^3 \geq 0$, thus for

$$\bar{\lambda} \leq \bar{\lambda}^{\text{crit}} = \frac{1}{4} \left(\frac{r_{\min}}{d}\right)^3 (-\bar{\varepsilon})^{-1}. \quad (15)$$

1. Einstein rings

The Einstein ring with radius $\theta_E \geq 0$ occurs when the source, lens and observer are on the same axis. The numerical solution of Eqs. (6), (10) and (11) with the conditions $\beta = 0$ and $s = 1$ gives $(\theta_E, r_{\min}/d, \delta)$ as functions of the parameters $\bar{\lambda}$ and $\bar{\varepsilon}$. The radius of the ring is represented on Fig. 2 for the particular configuration $D_{LS}/D_L = 2$. For $\bar{\lambda} \rightarrow 0$ we get the Schwarzschild lensing (the half-parabola shaped section of the surface with the largest opening with respect to the $\theta = 0$ plane). As $\bar{\lambda}$ increases, the opening of the half-parabola decreases, indicating the weakening of gravity (for a given $\bar{\varepsilon}$). At sufficiently large $\bar{\lambda}$ the contribution of $\bar{\varepsilon}$ becomes irrelevant and the geometry flattens, rendering the radius of the Einstein ring $\theta_E \rightarrow 0$. For a given mass and lensing geometry, the Einstein angles in the Kehagias-Sfetsos space-time are always smaller than their Schwarzschild value.

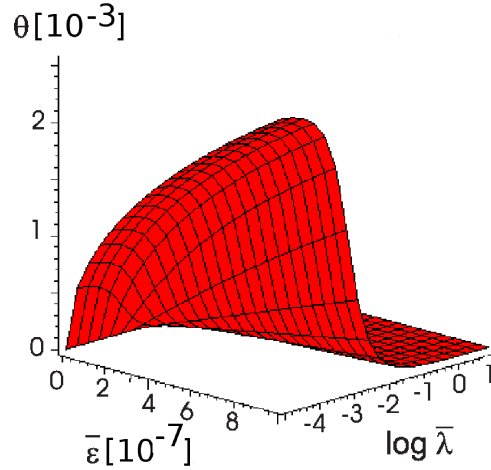


FIG. 2: The radius of the Einstein ring as function of the mass parameter $\bar{\epsilon}$ and Hořava-Lifshitz parameter $\bar{\lambda}$ for the Kehagias-Sfetsos space-time, assuming $D_{LS}/D_L = 2$. For $\bar{\lambda} \rightarrow 0$ we reobtain the Schwarzschild result. With increasing $\bar{\lambda}$, as the metric approaches flatness, the radius of the Einstein ring shrinks, and tends to zero for large values of $\bar{\lambda}$.

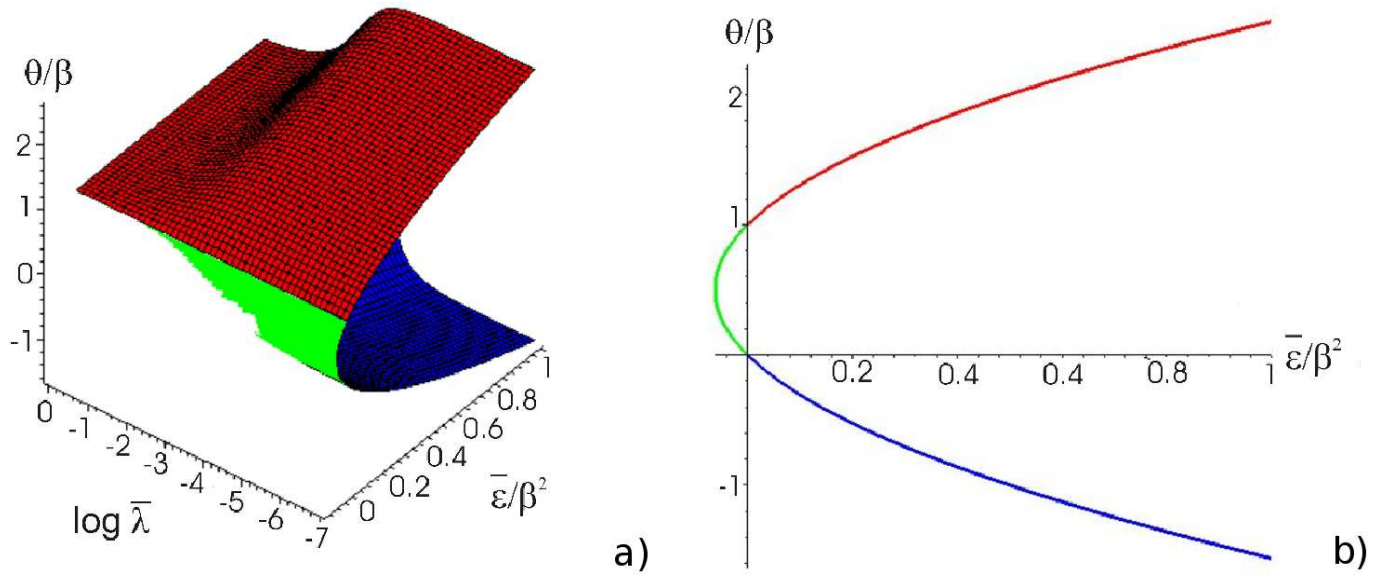


FIG. 3: The position of the images as function of the mass parameter $\bar{\epsilon}$ and Hořava-Lifshitz parameter $\log \bar{\lambda}$ for the Kehagias-Sfetsos space-time (with $D_{LS}/D_L = 2$ and $\beta = 10^{-3}$ rad) is represented on panel a). The three surfaces on the figure refer to: (1) the focused positive image is represented by the upper (red) surface; (2) the focused negative image is seen underneath (blue); (3) the scattered images (with $0 < \theta < \beta$) are found in the junction of the two surfaces mentioned generated by a negative mass (green). For $\bar{\lambda} \rightarrow 0$ we reobtain the Schwarzschild result, the parabola shown on panel b). With increasing $\bar{\lambda}$ only the positive focused image is left. For very large $\bar{\lambda}$, the metric approaches flatness.

2. Images

For generic positions $\beta > 0$, the numerical solving code for Eqs. (6), (10) and (11) calculates $(\theta/\beta, r_{\min}/d, \delta)$ as a function of the parameters $\bar{\lambda}$ and $\bar{\epsilon}$. The image positions (in units β , thus represented as θ/β) for a range of masses (represented as $\bar{\epsilon}/\beta^2$) are plotted on Fig. 3 (color online). The three surfaces on the figure refer to the following situations: (1) the focused positive image is represented by the upper surface (red in color version); (2) the focused negative image is seen underneath (blue); (3) the scattered images (with $0 < \theta < \beta$) are found in the junction of the two surfaces mentioned generated only the positive focused image is left. For very large $\bar{\lambda}$, the metric approaches flatness.

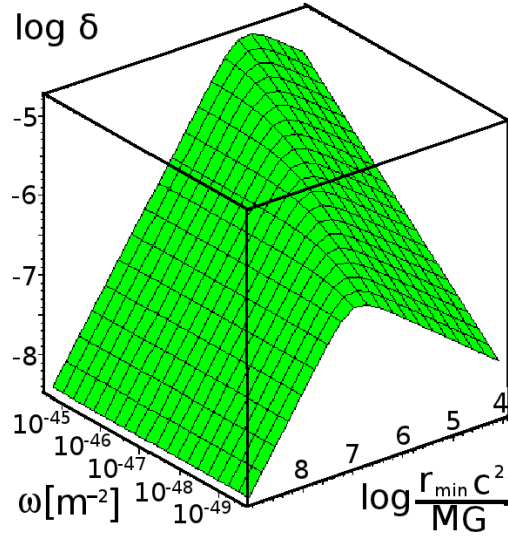


FIG. 4: The logarithm of the deflection angle δ as function of the distance of minimal approach (represented in units m , on logarithmic scale) and Hořava-Lifshitz parameter ω . The represented range of ω corresponds to the range of $\bar{\lambda}$ of Fig 3, when the lens mass is $m = 4.284 \cdot 10^{14}$ meter, $D_S = 4.190 \cdot 10^{25}$ meter and $D_{LS}/D_L = 2$. For every ω there is a maximal deflection angle δ_{\max} , corresponding to certain r_{crit} . The critical r_{crit} distance decreases with increasing ω . (Near the Schwarzschild limit r_{crit} shelters below the horizon and tends to 0 when $\omega \rightarrow \infty$, resulting the well known decreasing $\delta(r_{\min})$ function out of the horizon.) Rays passing both above and below r_{crit} will experience less deflection than δ_{\max} .

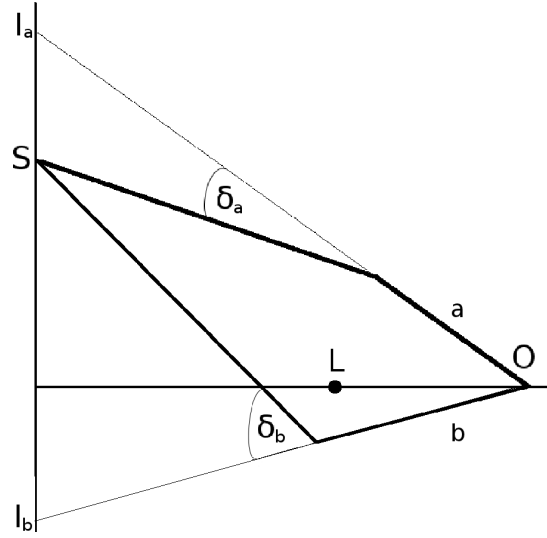


FIG. 5: The lensing geometry and rays labeled (a) and (b) for a large ω , reproducing image formation in Schwarzschild space-time, with two images I_a and I_b of the source S . The deflection angles obey $\delta_{(b)} > \delta_{(a)}$.

negative masses, where no image is formed at all (see (15)).

The parabolic edge of the represented surface (the parabola with the largest opening given by the $\bar{\lambda} = 0$ section) corresponds to image formation by weak lensing in the Schwarzschild limit of the Kehagias-Sfetsos space-time. As we increase $\bar{\lambda}$, a similar evolution of the loci of the positive focused images occurs, as for the radius of the Einstein ring: the images come closer to the optical axis. Increasing $\bar{\lambda}$ even more leads to a surprising situation: the negative image suddenly disappears (the lower surface has a sharp edge, when $\bar{\lambda} \rightarrow \mathcal{O}(10^{-3})$). We will explain this phenomenon below. Finally, for sufficiently large $\bar{\lambda}$ the space-time flattens and $\theta/\beta \rightarrow 1$, corresponding to no deflection at all.

In order to explain what happens in Fig 3 at intermediate values of $\bar{\lambda}$ first we have to study the behavior of the deflection angle δ as function of the distance of closest approach r_{\min} . This is depicted in Fig 4 for various parameter values ω corresponding to the intermediate $\bar{\lambda}$ range. We find that (a) at a certain r_{\min} the deflection angle decreases with ω , and (b) there is a maximal deflection angle δ_{\max} , corresponding to certain r_{crit} . Rays passing both above and

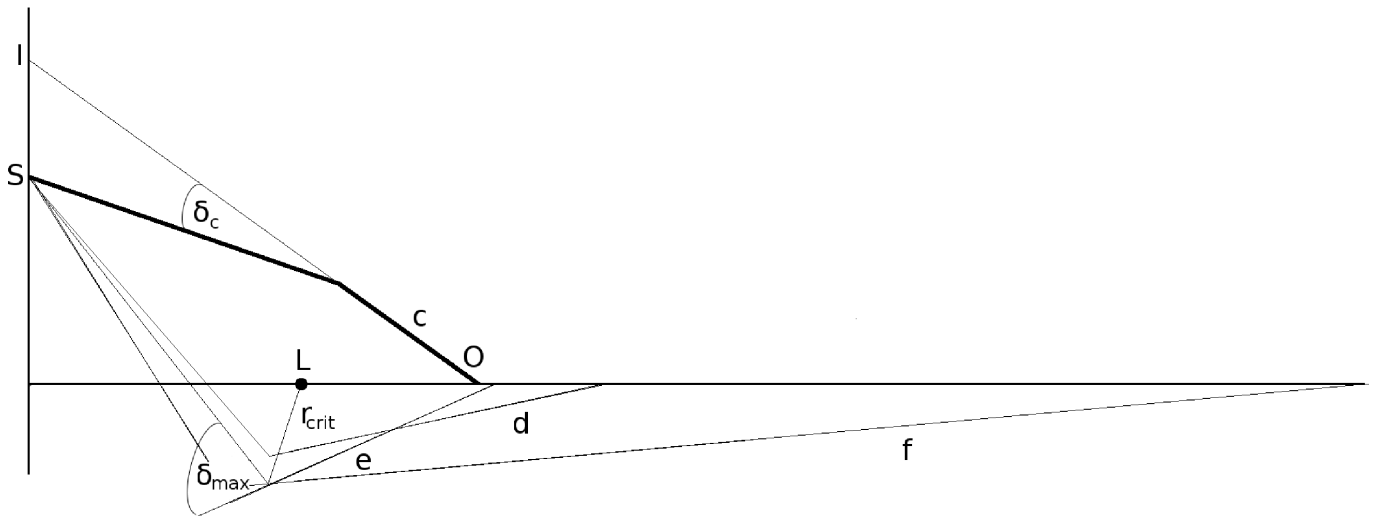


FIG. 6: The lensing geometry and rays for an ω producing a small enough value of δ_{\max} , such as the upper image (c) is formed, however no lower image appears, as the ray (e) passing through r_{crit} will intersect the optical axis farther than the observer. All rays passing below the lens, irrespectively whether their r_{\min} is smaller (d) or larger (f) than r_{crit} will intersect the optical axis at even larger distance.

below r_{crit} will experience less deflection, than the one passing through r_{crit} .

Rays captured by the observer which pass below the lens should exhibit a larger deflection angle, than the ones passing above the lens, see Fig 5. However for each source-lens-observer geometry there will be a value of ω for which the corresponding δ_{\max} will not be sufficient to deflect any of the rays passing below the lens to the observer. Hence the lower image disappears. This feature is illustrated in Fig 6. Similar considerations hold for the negative mass region.

We conclude that light deflection by weak gravitational lensing typically produces two images, as in Schwarzschild lensing, if ω is very large. For any fixed source-lens-observer geometry there is an intermediate value range of ω -s for which only the upper image exists. Finally, as we have already emphasized, a sufficiently large $\bar{\lambda}$ renders the space-time close to flat.

III. EINSTEIN ANGLES AND THE KEHAGIAS-SFETSOS PARAMETER

The Large Synoptic Survey Telescope (LSST) is expected to discover a high number of gravitational lenses, allowing statistical studies [17]. An advantage of LSST will be its excellent image quality [17]. The high resolution is crucial for lens searches, as the typical angular scales of lensing are comparable to the seeing sizes of ground-based observations (Fig 12.3 in [17]). The lens galaxy population is expected [17] to be dominated by massive elliptical galaxies at redshift 0.5-1, whose background light sources are the faint blue galaxies. Therefore the detection of such systems depends on the ability to distinguish lens light from the source light [17]. Fig 12.6 in [17] shows how the detection rate of galaxy lenses depends on image quality. The best predicted seeing presented in the figure is 0.3 arcsec. According to Fig 12.5 in [17] the median seeing is about half of that of the SDSS (Sloan Digital Sky Survey), which is 1.4 arcsec.

The Sloan Lens Advanced Camera and Spectrograph Survey (SLACS) has provided the largest sample of galaxy-scale lenses to date, with almost 100 lenses detected and measured [18]. The sources are faint blue galaxies, selected by their emission lines appearing in the lower redshift SDSS luminous red galaxy spectra. The largest collection of gravitational lens systems of SLACS was analyzed in [19]. SLACS is a project that combines the massive data volume of the SDSS with the high-resolution imaging capability of the Hubble Space Telescope (HST) to identify and study a large and uniform sample of gravitational lens galaxies. The lens galaxies are selected from the spectroscopic database of the SDSS for the presence of two galaxies along the same line of sight in the sky, one much more distant than the other.

The HST images allow us to measure the angular size of the Einstein rings. The observed Einstein angles are given in Table 1 in [19], they range from 0.69 arcsec to 1.78 arcsec. These angles combining with the distances measured from the SDSS spectra give us direct measurements of the enclosed masses of the nearer galaxies (the lens galaxies). The ACS-WFC (Advanced Camera for Surveys, Wide Field Channel) instrument was used for measurement of the

galaxy	θ_E [arcsec]	M [$10^{10} M_\odot$]	D_L [Mpc]	D_S [Mpc]	r_{\min} [Kpc]	ω_{\min} [10^{-48} cm^{-2}]	$\omega_{0,\min}$ [10^{-16}]
J0008-0004	1.16	35	1172.743	1708.956	6.595	0.18942	5.0657
J0029-0055	0.96	12	750.391	1622.253	3.492	0.27033	0.84982
J0037-0942	1.53	29	669.889	1411.834	4.969	0.34628	6.3576
J0044+0113	0.79	9	446.200	672.576	1.709	1.2219	2.1606
J0109+1500	0.69	13	905.964	1291.699	3.031	0.33425	1.2332
J0157-0056	0.79	26	1276.277	1618.923	4.888	0.23749	3.5047
J0216-0813	1.16	49	984.161	1289.158	5.535	0.35670	18.697
J0252+0039	1.04	18	875.400	1644.710	4.414	0.22816	1.6138
J0330-0020	1.10	25	1020.790	1676.984	5.444	0.20053	2.7361
J0405-0455	0.80	3	293.680	1555.222	1.139	1.1703	0.22993
J0728+3835	1.25	20	696.489	1463.700	4.221	0.32141	2.8066
J0737+3216	1.00	29	964.236	1358.283	4.675	0.30324	5.5673
J0822+2652	1.17	24	784.904	1372.544	4.452	0.30991	3.8969
J0903+4116	1.29	45	1157.167	1675.061	7.237	0.19736	8.7248
J0912+0029	1.63	40	580.506	968.258	4.587	0.60497	21.131
J0935-0003	0.87	41	1013.21	1213.066	4.274	0.48386	17.756
J0936+0913	1.09	15	653.631	1366.016	3.454	0.36699	1.8026
J0946+1006	1.38	29	737.793	1388.471	4.936	0.32025	5.87966
J0956+5100	1.33	37	782.476	1217.394	5.045	0.37351	11.163
J0959+4416	0.96	17	775.156	1299.251	3.608	0.33752	2.1294
J0959+0410	0.99	8	465.339	1304.229	2.233	0.58732	0.82058
J1016+3859	1.09	15	592.045	1171.202	3.129	0.47174	2.3171
J1020+1122	1.20	34	879.827	1326.068	5.119	0.31376	7.9181
J1023+4230	1.41	23	656.356	1470.562	4.487	0.34248	3.9551
J1029+0420	1.01	6	393.820	1394.687	1.928	0.73490	0.57756
J1100+5329	1.52	47	954.102	1584.325	7.031	0.22552	10.875
J1106+5228	1.23	9	366.879	1119.963	2.188	0.90303	1.5968
J1112+0826	1.49	45	859.747	1408.858	6.211	0.28347	12.531
J1134+6027	1.10	13	548.213	1223.120	2.924	0.49304	1.8190
J1142+1001	0.98	17	737.793	1264.429	3.505	0.36081	2.2764
J1143-0144	1.68	19	400.476	1111.614	3.262	0.79571	6.2708
J1153+4612	1.05	11	626.027	1593.810	3.187	0.34366	0.90778
J1204+0358	1.31	17	580.506	1410.844	3.687	0.41199	2.5993
J1205+4910	1.22	25	719.910	1233.014	4.258	0.37895	5.1705
J1213+6708	1.42	14	455.803	1419.669	3.138	0.7912	2.4779
J1218+0830	1.45	16	493.548	1487.965	3.470	0.5017	2.8041
J1250+0523	1.13	18	762.845	1545.386	4.179	0.27744	1.9624
J1402+6321	1.35	29	693.857	1233.014	4.541	0.38808	7.1250

TABLE I: Column 1: the lens galaxies. Column 2-5: the Einstein angle θ_E , total lens mass inside the Einstein radius R_E , the distances D_L and D_{LS} . The quantities calculated from the model are r_{\min} (column 6), ω_{\min} and $\omega_{0,\min} := G^2 M_{lum+dark}^2 \omega_{\min} / c^4$ (columns 7 and 8).

Einstein angles [18]. This channel will be optimized for surveys in the near-infrared to search for galaxies and clusters in the early universe, and possesses 0.049 arcsec pixel size [20]. The SLACS sample is currently the largest collection of gravitational lens systems with known distances (redshifts) to both components.

The photometric and spectroscopic measurements for the 57 massive early-type lens galaxies discussed in [19] are available from SDSS. By using multicolor photometry and lens models, [19] studied stellar-mass properties and the luminous and dark matter composition of the early-type lens galaxies. The fraction of mass in the form of stars of the selected early-type grade-A lens galaxies in the sample was also presented.

Astronomical angle measurements come with certain uncertainty $\Delta\theta$, which allow for a range $\omega \in (\omega_{\min}, \infty)$ of the Hořava-Lifshitz parameter, where ω_{\min} obeys $\theta_E(\omega_{\min}) = \theta_{E,Sch} - \Delta\theta$. For any such ω the Einstein angle would be

galaxy	θ_E [arcsec]	M [$10^{10} M_\odot$]	D_L [Mpc]	D_S [Mpc]	r_{\min} [Kpc]	ω_{\min} [10^{-48} cm^{-2}]	$\omega_{0,\min}$ [10^{-16}]
J1403+0006	0.83	10	650.899	1221.693	2.619	0.41355	0.90280
J1416+5136	1.37	37	916.645	1555.865	6.088	0.23665	7.0726
J1420+6019	1.04	4	250.179	1304.222	1.261	1.6168	0.56474
J1430+4105	1.52	54	886.429	1351.555	6.532	0.30198	19.224
J1436-0000	1.12	23	886.429	1551.984	4.813	0.24263	2.8020
J1443+0304	0.81	6	490.443	1139.617	1.926	0.59752	0.46959
J1451-0239	1.04	8	462.168	1285.325	2.330	0.59786	0.83530
J1525+3327	1.31	48	1033.889	1487.965	6.566	0.25047	12.598
J1531-0105	1.71	27	568.859	1509.087	4.716	0.40490	6.4438
J1538+5817	1.00	9	518.128	1299.251	2.512	0.50680	0.89616
J1621+3931	1.29	29	794.563	1381.108	4.969	0.30476	5.5953
J1627-0053	1.23	23	701.736	1290.430	4.185	0.36381	4.2014
J1630+4520	1.78	49	801.749	1544.046	6.919	0.26412	13.844
J1636+4707	1.09	18	752.893	1451.370	3.979	0.29974	2.1201
J2238-0754	1.27	13	499.736	1484.718	3.077	0.49325	1.8198
J2300+0022	1.24	30	755.390	1208.707	4.541	0.38187	7.5028
J2303+1422	1.62	27	554.146	1281.465	4.352	0.46848	7.4556
J2321-0939	1.60	12	318.486	1300.500	2.470	1.0661	3.3514
J2341+0000	1.44	22	642.666	1553.284	4.487	0.33734	3.5644

TABLE II: Table I continued.

TABLE III: Radii of the first and second relativistic Einstein rings, with corresponding ω_{\min} and $\omega_{0,\min}$ for $\Delta\theta_E = 10^{-5}$ arcsec.

Einstein ring	$\theta_{E,Sch}$ [10^{-5} arcsec]	ω_{\min} [cm^{-2}]	$\omega_{0,\min}$
1 st relativistic	2.557	$8.1315 \cdot 10^{-25}$	0.3282
2 nd relativistic	2.554	$8.1315 \cdot 10^{-25}$	0.3282

observationally indistinguishable from the Schwarzschild value $\theta_{E,Sch}$. By contrast, every $\omega < \omega_{\min}$ correspond to Einstein rings outside the measurement accuracy. In the following we take the accuracy of SDSS, $\Delta\theta = 0.049$ arcsec.

In Tables I and II column 2 gives the Einstein angles of the lens galaxies enlisted in column 1, with the total (dark + luminous) masses falling inside the effective Einstein radius $R_E = D_L\theta_E$ given in column 3 [19]. We have converted the redshifts z_L , z_S of the lens and the source galaxies given in Table 1 in [19] to the angular diameter distances D_L , D_{LS} (columns 4, 5) using the value $H_0 = 70$ km/s/Mpc for the Hubble parameter and $\Omega_\Lambda = 0.7$, $\Omega_M = 0.3$ for the cosmological parameters.

We confronted all these data with the weak lensing equations in the Kehagias-Sfetsos space-time, obtaining numerically the values of r_{\min} , ω_{\min} and $\omega_{0,\min} := (GM_{lum+dark}/c^2)^2 \omega_{\min}$, given in columns 6, 7, 8. We will compare these values with other constraints existing in the literature in the Conclusion Section, basically finding agreement with other type of constraints.

IV. STRONG LENSING IN THE KEHAGIAS-SFETSOS SPACE-TIME

Relativistic images are not observed yet, however the Multi-AO Imaging Camera for Deep Observations (MICADO) - to function from 2018, using adaptive optics, on the 42 m European Extremely Large Telescope - is designed to have a resolution in the astrometric mode of about 10^{-5} arcsec [21, 22]. This resolution is close to the scale of the relativistic images.

This will allow to constrain the quantities ω and ω_0 in the strong lensing configuration, suggested for testing the Schwarzschild space-time in Ref. [23]. In this configuration the lens is the Supermassive Black Hole in the center of our galaxy, Sagittarius A*, with mass $4.3 \times 10^6 M_\odot$, and the light is coming from a stellar source on the opposite side of the galaxy, such that the distances of the lens and the source are $D_L = 8.3$ kpc and $D_S = 2D_L$. Next we apply the method of constraining ω_0 developed in the previous section for this configuration and the expected resolution of MICADO.

The results are presented in Table III. The rows refer to the first and second relativistic Einstein rings, respectively, as calculated in the Schwarzschild space-time (column 2). Columns 3 and 4 contain the lower limit of ω and ω_0 arising from the envisaged resolution of $\Delta\theta = 10^{-5}$ arcsec. Although several orders of magnitude larger than presently available limits, this value of $\omega_{0,\min}$ would still allow for the galactic Supermassive Black Hole to be a naked singularity, as the black hole conditions $\omega_0 > 1/2$ and (14) are disobeyed. A further slight decrease in $\Delta\theta$ would be necessary in order to disrule this possibility.

V. CONCLUSION

In this paper, we discussed the image formation in both weak and strong gravitational lensing by the Kehagias-Sfetsos solution in the framework of Hořava-Lifshitz gravity. Such a gravitational lens is characterized by a mass-type parameter $\bar{\varepsilon}$ and an additional parameter $\bar{\lambda}$. The overbar denotes certain scaling of these dimensionless parameters with a characteristic length d characterizing the geometry. The Schwarzschild limit occurs when $\bar{\lambda} \rightarrow 0$, while in the limit $\bar{\lambda} \rightarrow \infty$ the Kehagias-Sfetsos space-time becomes flat (the contribution of an increasing $\bar{\lambda}$ cancels the gravitational attraction of the positive $\bar{\varepsilon}$). There is also an intermediate range, characterized by the existence of a maximal deflection angle δ_{\max} , occurring at r_{crit} . This means that both the rays passing closer and farther to the lens than r_{crit} will experience less deflection.

In the weak lensing approximation a closed system of equations for the variables θ (image position), r_{\min} (distance of minimal approach) and δ (deflection angle) is given by the lens equation relating θ and δ to each other, an integral formula to produce δ as a function of r_{\min} and a third equation which connects r_{\min} to the impact parameter $b = D_L \sin(s\theta)$. We have employed the Virbhadra-Ellis lens equation, presenting sufficient accuracy for our first order approach. For the deflection angle we adopted the improper integral given in Ref. [11], then performed a transformation which removes the singularity at $r = r_{\min}$, allowing the numerical integration. Finally we employed the algebraic relation (10) connecting θ and r_{\min} given in Ref. [15].

The aligned case $\beta = 0$ leads to the formation of Einstein rings. These Einstein angles were plotted as functions of the space-time parameters $\bar{\varepsilon}$ and $\bar{\lambda}$ in Fig 2. For $\bar{\lambda} \rightarrow 0$ we recovered the half-parabola shaped section of the surface, representing the Schwarzschild limit of weak lensing. As $\bar{\lambda}$ increases, the opening of the half-parabola decreases, indicating a weakening of gravity.

For source positions $\beta > 0$ the surface representing the image positions, shown in Fig 3a, is more complex. We showed that in the weak gravitational lensing regime, the light deflection either produces two images, as in Schwarzschild lensing, or only one image. In the latter case the existence of δ_{\max} is obstructing the creation of the lower image. As $\bar{\lambda}$ increases further, the space-time flattens and $\theta/\beta \rightarrow 1$, which causes that the $\theta > 0$ (upper, red) surface on Fig 3a flattens as well. When $\bar{\lambda} \rightarrow \mathcal{O}(10^{-3})$ the $\theta < 0$ (lower, blue) branch has a sharp edge and disappears. As a further consequence the middle (green) surface representing the two scattered images occurring for negative masses also disappear for $\bar{\lambda} \rightarrow \infty$. As in the Schwarzschild case, there is a parameter region encompassing only negative masses, where no image is formed at all.

We also analyzed the photometric and spectroscopic measurements for a sample of 57 lens galaxies available from SDSS, given in Ref. [19]. These led to estimates of masses and lensing distances. From the observed locations of the corresponding Einstein rings and the accuracy of measurements we derived the range of the Hořava-Lifshitz parameter $\omega = \bar{\lambda}^{-1}d^{-2}$ characterizing the Kehagias-Sfetsos space-time compatible with the observations. The results are presented in Tables I, II. The dimensionless quantity $\omega_{0,\min} := (GM_{lum+dark}/c^2)^2 \omega_{\min}$ for the sample of lens galaxies is typically found to be of the order 10^{-16} .

We compare these numbers with related results in the literature. In Ref. [5] the Solar System tests were analyzed, imposing constraints on ω_0 from the available observations. Perihelion precession of the planet Mercury, deflection of light by the Sun and the radar echo delay gave, respectively the limits $\omega_{0,\min}^{(pp)} = 6.9 \times 10^{-16}$, $\omega_{0,\min}^{(ld)} = 1.1 \times 10^{-15}$, and $\omega_{0,\min}^{(red)} = 2 \times 10^{-15}$, respectively. In Ref. [24] the weak-field and slow-motion approximation was employed to compare with the orbital periods of the transiting extrasolar planet HD209458b (Osiris), obtaining a weaker bound of $\omega_0^{(Osiris)} = 1.4 \times 10^{-18}$. In Ref. [25], constraints on Hořava-Lifshitz gravity from light deflection observations including long-baseline radio interferometry, Jupiter measurement, Hipparcos satellite are found also in the range of $\omega_0^{(radio)} \in 10^{-15} \div 10^{-17}$. Our findings are therefore consistent with these results. Stronger bounds of $\omega_0^{(residual)} = 7.2 \times 10^{-10}$ were presented from the accurate data of range-residuals of the planet Mercury ranged from the Earth, and $\omega_0^{(Sag)} = 8 \times 10^{-10}$ for the system constituted by the S2 star orbiting the Supermassive Black Hole (Sagittarius A*) in the center of the Galaxy [26]. We stress however, that the latter value of $\omega_0^{(Sag)}$ would render our galactic Supermassive Black Hole into a naked singularity, as the condition $\omega_0 > 1/2$ is disobeyed.

Finally, we discussed the first two relativistic Einstein rings in the strong lensing regime. Applying to the galactic

center as a strong lens and a light source located on the opposite side, a configuration discussed in Ref. [23], we determined the constraints on ω_0 , given in Table III (under the assumption of fixed lens mass) arising from the expected accuracy of 10^{-5} arcsec of future instruments [22]. We found that such measurements would constrain quite severely the parameter range, up to $\omega_{0,\min}$ of order 10^{-1} , allowing to either falsify the Hořava-Lifshitz theory or to render the parameter of the Kehagias-Sfetsos space-time into a regime where it practically becomes indistinguishable from the Schwarzschild space-time. This would set the strongest observational constraint on the Hořava-Lifshitz parameter up to date.

VI. ACKNOWLEDGMENTS

L. Á. G. and F. S. N. L. would like to thank the Department of Physics of The University of Hong Kong for their support and warm hospitality during the preparation of this work. Zs. H. was supported by the European Union and co-funded by the European Social Fund through the TÁMOP 4.2.2/B-10/1-2010-0012 grant. L. Á. G. was partially supported by COST Action MP0905 “Black Holes in a Violent Universe”. The work of T. H. was supported by the General Research Fund grant number HKU 701808P of the government of the Hong Kong Special Administrative Region. F. S. N. L. acknowledges financial support of the Fundação para a Ciência e Tecnologia through the grants PTDC/FIS/102742/2008, CERN/FP/109381/2009 and CERN/FP/116398/2010.

-
- [1] P. Hořava, JHEP **0903**, 020 (2009).
 - [2] P. Hořava, Phys. Rev. **D79**, 084008 (2009).
 - [3] M. Visser, arXiv:1103.5587 [hep-th] (2011).
 - [4] R. A. Konoplya, Phys. Lett. **B679**, 499 (2009); S. Chen and J. Jing, Phys. Rev. **D80**, 024036 (2009); J. Chen, Y. Wang, arXiv:0905.2786 [gr-qc]; T. Harko, Z. Kovacs, F. S. N. Lobo, Phys. Rev. **D80**, 044021 (2009).
 - [5] T. Harko, Z. Kovacs, F. S. N. Lobo, Proc. Roy. Soc. Lond. A Math. Phys. Eng. Sci. **467**, 1390 (2011); F. S. N. Lobo, T. Harko, Z. Kovacs, Class. Quant. Grav. **28**, 165001 (2011).
 - [6] A. Kehagias, K. Sfetsos, Phys. Lett. **B678**, 123 (2009).
 - [7] Z. Horváth, L. Á. Gergely, D. Hobill, Class. Quant. Grav. **27**, 235006 (2010).
 - [8] K. S. Virbhadra, G. F. R. Ellis, Phys. Rev. **D62**, 084003 (2000).
 - [9] K. S. Virbhadra, Phys. Rev. **D79**, 083004 (2009).
 - [10] C. Darwin, Proc. R. Soc. London **A249**, 180 (1959); **A263**, 39 (1961); R. Atkinson, The Astronomical Journal, 70, 517 (1965); K. P. Rauch, R. D. Blandford, Astrophys. J. **421**, 46 (1994); K. S. Virbhadra, D. Narasimha, S. M. Chitre, Astron. Astrophys. **337**, 1 (1998); K. S. Virbhadra, G. F. R. Ellis, Phys. Rev. **D65**, 103004 (2002); K. S. Virbhadra, C. R. Keeton, Phys. Rev. **D77**, 124014 (2008).
 - [11] S. Weinberg, *Gravitation and Cosmology*, Principles and Applications of the General Theory of Relativity, New York, Wiley (1972).
 - [12] J. Greenwald, J. Lenells, J. X. Lu, V. H. Satheeshkumar, A. Wang, arXiv:1105.4259v2 [hep-th] (2011).
 - [13] E. Barausse, T. Jacobson, T. P. Sotiriou, Phys. Rev. **D83**, 124043 (2011).
 - [14] A. E. Mosaffa, Phys. Rev. **D83**, 124006 (2011).
 - [15] L. Á. Gergely, Z. Keresztes, M. Dwornik, Class. Quant. Grav. **26**, 145002 (2009).
 - [16] V. Bozza, Phys. Rev. **D78**, 103005 (2008).
 - [17] LSST Science Collaborations, *LSST Science Book Version 2.0* (2009), www.lsst.org/lsst/scibook, arXiv:0912.0201.
 - [18] A. S. Bolton, S. Burles, L. V. E. Koopmans, T. Treu, L. A. Moustakas, Astrophys. J. **638** 703 (2006).
 - [19] C. Grillo, R. Gobat, M. Lombardi, P. Rosati, Astron. Astroph. **501**, 461 (2009).
 - [20] S. Gonzaga et al., *ACS Data Handbook Version 6.0* (Baltimore, STScI, 2011), www.stsci.edu/hst/acs/documents/handbooks/currentDHB.
 - [21] A. Bin-Nun, Class. Quantum Grav. **28**, 114003 (2011).
 - [22] S. Trippe et. al., Mon. Not. Royal Astron. Soc. **402**, 1126 (2010).
 - [23] A. Bin-Nun, Phys. Rev. **D81**, 123011 (2010).
 - [24] L. Iorio, M. L. Ruggiero, Int. J. Mod. Phys. **D20**, 1079 (2011).
 - [25] M. Liu, J. Lu, B. Yu, J. Lu, Gen. Rel. Grav. **43**, 1401 (2010).
 - [26] L. Iorio, M. L. Ruggiero, Open Astron. J. **3**, 167 (2010).